Finite Elements in Analysis and Design 241 (2024) 104239

Contents lists available at ScienceDirect

Finite Elements in Analysis & Design

journal homepage: www.elsevier.com/locate/finel

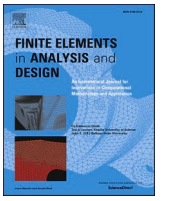

Finite element modeling of thermal residual stresses in functionally graded aluminum-matrix composites using X-ray micro-computed tomography

Witold Węglewski [a,*], Anil A. Sequeira [a], Kamil Bochenek [a], Jördis Rosc [b], Roland Brunner [b], Michał Basista [a]

[a] Institute of Fundamental Technological Research, Polish Academy of Sciences, Pawińskiego 5B, 02-106, Warsaw, Poland
[b] Materials Center Leoben Forschung GmbH, Roseggerstrasse 12, 8700, Leoben, Austria

ARTICLE INFO

Keywords:
Finite element modeling
Micro-XCT
Thermal residual stress
Hot pressing
Aluminum matrix composites

ABSTRACT

Metal-ceramic composites by their nature have thermal residual stresses at the micro-level, which can compromise the integrity of structural elements made from these materials. The evaluation of thermal residual stresses is therefore of continuing research interest both experimentally and by modeling. In this study, two functionally graded aluminum alloy matrix composites, AlSi12/Al_2O_3 and AlSi12/SiC, each consisting of three composite layers with a stepwise gradient of ceramic content (10, 20, 30 vol%), were produced by powder metallurgy. Thermal residual stresses in the AlSi12 matrix and the ceramic reinforcement of the ungraded and graded composites were measured by neutron diffraction. Based on the X-ray micro-computed tomography (micro-XCT) images of the actual microstructure, a series of finite element models were developed to simulate the thermal residual stresses in the AlSi12 matrix and the reinforcing ceramics Al_2O_3 and SiC. The accuracy of the numerical predictions is high for all cases considered, with a difference of less than 5 % from the neutron diffraction measurements. It is shown numerically and validated by neutron diffraction data that the average residual stresses in the graded AlSi12/Al_2O_3 and AlSi12/SiC composites are lower than in the corresponding ungraded composites, which may be advantageous for engineering applications.

1. Introduction

Thermal residual stresses are important in any metal-ceramic composite regardless of the specific application. In the case of Al/Al_2O_3 and Al/SiC composites, the amount of previous work on material properties and their relation to the microstructure is abundant (e.g., mechanical properties [1–3], thermal properties [4–6], effect of microstructure on residual stresses [7–9]). Previous studies of functionally graded materials (FGMs) focusing on the material behavior have often been limited to analytical or numerical approaches, while much less experimental work has been published, apparently due to the difficulty of fabricating FGMs and their complex microstructure, which makes experimental testing rather cumbersome. Thermal residual stresses (TRS) in functionally graded metal-ceramic composites can be measured using the same methods as for ungraded composites. Among the available non-destructive experimental methods, the most commonly used for metal-ceramic composites are X-ray diffraction (XRD) [10], synchrotron X-ray

* Corresponding author.
E-mail address: wweglew@ippt.pan.pl (W. Węglewski).

https://doi.org/10.1016/j.finel.2024.104239
Received 22 April 2024; Received in revised form 1 August 2024; Accepted 25 August 2024
Available online 31 August 2024

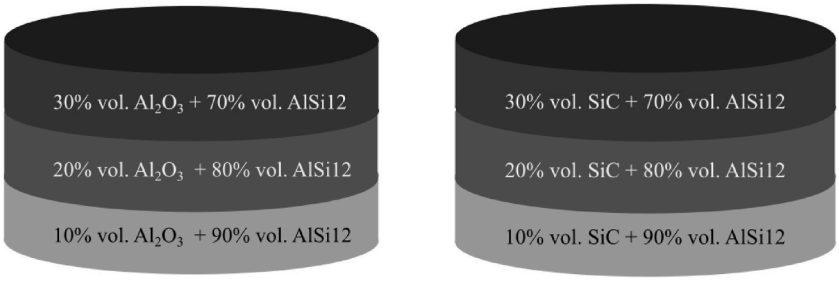

Fig. 1. Schematic of the three-layer graded materials (FGMs) studied in this work: (a) AlSi12/Al_2O_3, (b) AlSi12/SiC.

diffraction (SXD) [11], neutron diffraction (ND) [12], Raman spectroscopy (RS) and photoluminescence piezospectroscopy (PLPS) [13]. The basic principle of diffraction techniques is to measure elastic deformation and lattice distortion based on the shift and broadening of the diffraction peaks. X-rays, however, are well suited for measuring near-surface stresses because of their limited penetration depth for metals such as aluminum, which ranges from 30 μm to 100 μm [14]. For bulk metal-ceramic composites, the neutron diffraction method is more effective due to the high neutron penetration in most materials. The general disadvantage of all diffraction methods is that they are only applicable to crystalline solids, which is not the case with optical methods (RS, PLPS) [15]. Sometimes it is advantageous to use optical and diffraction methods in parallel to confirm unexpected experimental results on TRS in composites [16].

Experimental studies of the spatial variation of elastic modulus, compressive strength, and fracture toughness in a continuous FGM as a function of location to generate property profiles were described in a highly referenced paper [17]. The elastic constants and thermal expansion coefficients of the FGMs along the gradient directions were evaluated in Ref. [18]. The thermal conductivity of the FGM was measured by the laser flash method in Ref. [19] and compared with theoretical calculations for the layered material.

Although a distinction is usually made between continuous and discrete gradients for modeling purposes, the actual FGM microstructures are discrete and random. These highly inhomogeneous microstructures, when composed of thermally dissimilar materials (such as Al and SiC or Al_2O_3), can result in local residual stresses during fabrication or under thermal or mechanical loading in engineering applications. Locally concentrated stresses, especially tensile stresses, can initiate microcracks or voids, which can be detrimental to any material being considered for structural or functional applications [20]. Therefore, the modeling of residual stresses in FGMs is a top research priority.

Analytical approaches to model the thermal stresses in metal-ceramic composites often rely on the equivalent Eshelby inclusion method [21], which offers a closed-form solution for stresses generated by ellipsoidal dispersion in an elastic matrix. For example, a modified Eshelby model was developed in Refs. [22,23] to obtain analytical solutions for thermal residual stresses in ceramic-matrix composites with ellipsoidal reinforcement, and applied to special cases of disk-shaped, spherical or fiber-shaped reinforcement. However, when calculating thermal stresses in FGMs, a direct application of the Eshelby solution is not feasible because the RVE (Representative Volume Element) cannot be easily determined due to the spatial gradient of the microstructure. In continuous thermal residual stress models, the volume fraction gradient is first estimated from the rule of mixtures [24] or by assuming analytical functions (e.g., power law) for the changes in the elastic modulus of the FGM before proceeding to the heat transfer equation for the FGM [25].

Numerical models of thermal residual stresses in bulk composites (without gradation or with functional gradation) are now becoming popular because the actual shapes of the reinforcement, especially in composites produced by powder metallurgy techniques, do not lend themselves easily to analytical modeling [25]. The finite element analysis (FEA) has been used to solve the TRS problems for various types of inclusions. However, the complex domain discretization for composites requires many finite elements to obtain sufficiently accurate numerical solutions. Typical inclusion shapes such as spheres, fibers, or whiskers can be modeled using FEA software packages [26]. FEA has also been used to calculate thermal residual stresses in layered composites [27]. In this study, TRS models for layered FGMs are of particular interest due to the hot press consolidation technique used to obtain FGMs with a stepwise gradient in phase materials composition.

Experimental imaging methods such as X-ray micro-computed tomography (micro-XCT), synchrotron tomography and focused ion beam scanning electron microscopy (SEM-FIB) tomography are used in various fields [28–36] to image the microstructure in three dimensions. In addition, tomography-based microstructure data have also become attractive as an input for FEM modeling [37]. In general, the accurate reconstruction of the microstructure is a critical step for FEM modeling. However, by using the digital representative volume of the actual microstructure for modeling, assumptions about the microstructure of the material can be avoided. On the other hand, these experimental techniques have their limitations, as pointed out in Ref. [38]. Once an accurate digital representation of the microstructure is available, FEM models based on micro-XCT are quite effective in predicting thermal residual stresses [39,40] and elastic properties [41] in metal-ceramic composites.

The objectives of this work are: (i) to develop finite element models of the thermal residual stresses using the actual microstructures of the AlSi12/Al_2O_3 and AlSi12/SiC composites and FGMs reconstructed by 3D X-ray micro-tomography, (ii) to validate the micro-XCT based FEM models by comparing the numerical results with the experimental data obtained from the neutron diffraction experiments,

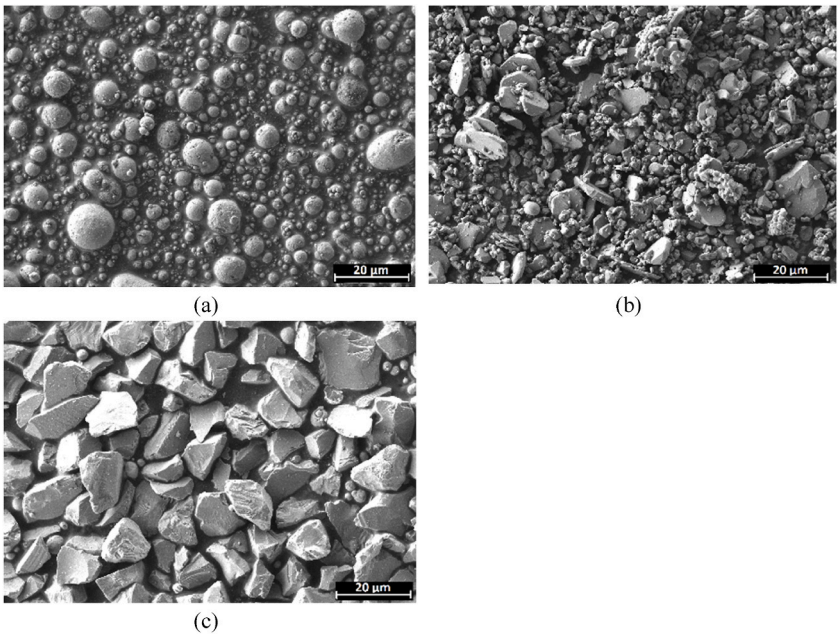

Fig. 2. SEM secondary electron detector images of as-received powders: (a) AlSi12, (b) Al_2O_3, (c) SiC.

(iii) to confirm that a graded structure of AlSi12/Al_2O_3 and AlSi12/SiC composites produced by powder metallurgy can reduce the process-induced thermal residual stresses in the metal matrix and the ceramic reinforcement.

2. Materials and methods

2.1. Materials preparation

Three-layer graded composites (FGMs) consisting of an aluminum alloy (AlSi12) matrix reinforced with aluminum oxide (Al_2O_3) or silicon carbide (SiC) particles were prepared by powder metallurgy. The graded structure and the volume composition of the AlSi12/Al_2O_3 and AlSi12/SiC bulk FGMs were the same. They consisted of three composite layers of equal thickness with 10, 20, and 30 vol% of ceramic particles (Al_2O_3 or SiC) embedded in the AlSi12 matrix as shown schematically in Fig. 1a and b.

The ungraded composites and the FGMs were fabricated in a similar manner. First, powder mixtures were prepared using the commercially available powders of AlSi12 alloy (NewMetKoch, average particle size 5 µm, purity 99.99 %), Al_2O_3 (Goodfellow, average particle size 10 µm, purity 99.99 %), and SiC (Goodfellow, average particle size 10 µm, purity 99.99 %). The particle size distribution of the powders AlSi12, Al_2O_3 and SiC was determined by laser diffraction using the Mastersizer 3000 particle size analyzer. The measured weight percentages of Al and Si in the AlSi12 alloy powder were 87.9 and 12.1 wt%, respectively. SEM images of as-received AlSi12, Al_2O_3, and SiC powders are shown in Fig. 2.

The mixing process was carried out in a planetary ball mill (Pulverisette 5, Fritsch) at a speed of 100 rpm, using 10 mm diameter tungsten carbide balls (ball-to-powder weight ratio BPR = 5:1). The total mixing time was 5 h, divided into mixing sessions in an inert gas atmosphere (argon) which lasted about 15 min and with cooling intervals of about 45 min. The consolidation process of the powder blends was performed in a cylindrical graphite mold with an inner diameter of 33 mm, placed in a hot press (Thermal Technology HP-20-4650) under a sintering temperature set at 560 °C, with a heating rate of 5 °C/min, sintering pressure of 30 MPa, and a dwell time of 3 h. Cooling to room temperature was performed in the mold without load.

Consolidation of the FGM samples was carried out by putting predefined volumes of the three powder blends in the mold and sintering them in one step. The thickness of each composite layer of the FGM was approximately 2 mm. It was determined from the volume of each powder which was calculated from the mass of the powder blend used and the theoretical densities of the constituent materials, assuming perfect compaction of the composite layers. As can be seen from Table 4 in Section 3.2, almost fully dense composites were achieved after optimization of the sintering process. The process parameters (i.e. sintering pressure, temperature, and dwelling time) for the FGMs were the same as for the ungraded composites.

2.2. Microstructure analysis

We characterized the microstructure of the fabricated composite materials by conducting scanning electron microscopy (SEM) experiments. The samples were cut one-fourth way across the diameter and along the thickness using a wire cutter. Next, the samples were ground and polished along the cross-sectional direction. The prepared samples were analyzed by using ZEISS Crossbeam 350

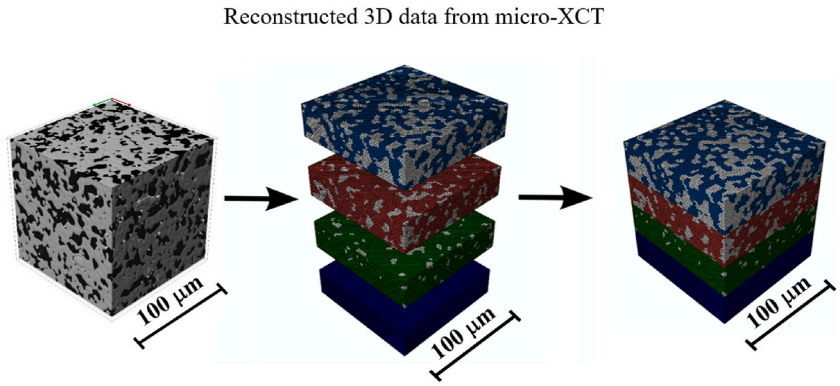

Fig. 3. Schematic of the microstructure reconstruction workflow illustrating the image processing steps. The left image shows the segmented XCT data. The middle image shows the meshing of the graded material from the micro-XCT scans for the volume of interest of 100 × 100 × 100 µm^3. The image on the right shows the meshed data used for residual stress modeling.

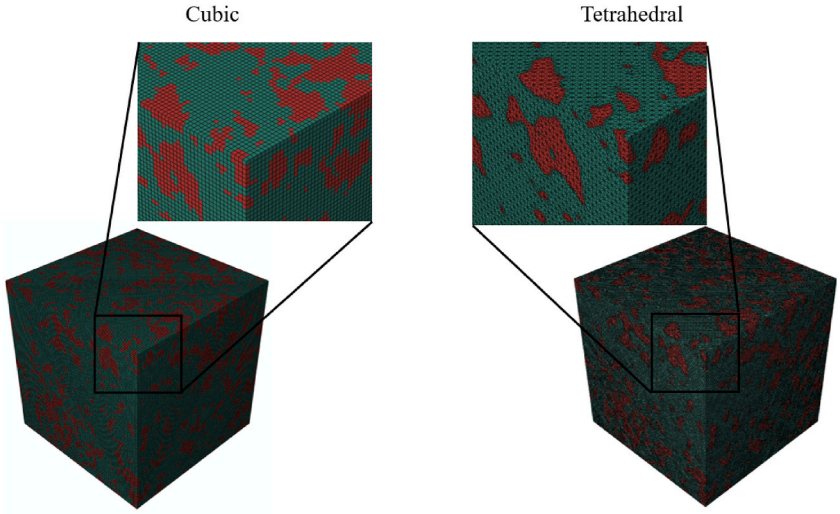

Fig. 4. Comparison of cubic (left) and tetrahedral (right) finite element meshes on an example of AlSi12 + 20%SiC composite.

Table 1
Volume fractions (vol%) of the ceramic reinforcement in the FE mesh models based on micro-XCT images.

	AlSi12 + 10% Al_2O_3	AlSi12 + 20% Al_2O_3	AlSi12 + 30% Al_2O_3	AlSi12 + 10% SiC	AlSi12 + 20% SiC	AlSi12 + 30% SiC
Al_2O_3 volume fraction in micro-XCT based FE mesh [%]	9.89	21.11	29.78	10.31	20.45	30.90

scanning electron microscope with a secondary electron detector and 5 kV voltage.

X-ray micro-computed tomography (micro-XCT) was performed and the three-dimensional images of the samples were reconstructed. The composite specimens prepared for micro-XCT experiments were cuboidal in shape, with the base of a square having a side of 1 mm and a height of approximately 10 mm. A volume of interest with 100 × 100 × 100 µm^3 was used for the meshing and subsequent numerical modeling of the thermal residual stresses. The micro-XCT experiments were performed on a Nanotom M (Phoenix/GE) system, with a voltage of 62 kV and a current of 230 µA. The voxel size was optimized with respect to image contrast and was set to about 1 × 1 × 1 µm^3. With these settings the imaging of the contours between the AlSi12 grains and the ceramic grains was feasible, a crucial condition for the subsequent segmentation and FE mesh generation.

2.3. Density measurement

The densities of the AlSi12/Al_2O_3 and AlSi12/SiC composite samples were measured by the Archimedes method. The theoretical

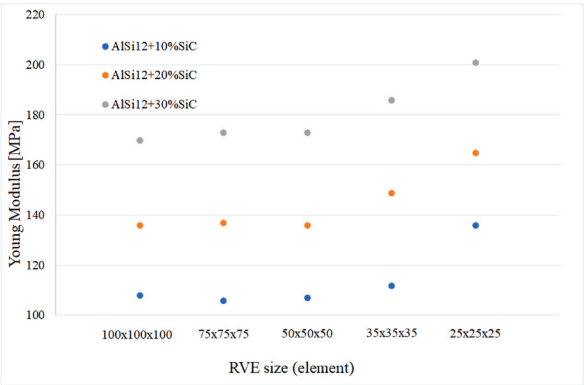

Fig. 5. Results of numerical calculations of Young's modulus for different RVE sizes (cubic elements).

Table 2
Elastic constants and coefficients of thermal expansion of the matrix and the reinforcing ceramics used in the FEM calculations.

Material constant	AlSi12	Al_2O_3	SiC
E (GPa)	70 [a]	380 [a]	410 [b]
Poisson's ratio	0.35 [25]	0.22 [b]	0.15 [b]
CTE (1/deg)	23.7×10^{-6} [a]	6.5×10^{-6} [a]	4.0×10^{-6} [b]

[a] Measured in-house on AlSi12 and Al_2O_3 sinters.
[b] Data from the powder producer.

Table 3
The data for the elasto-plastic material behavior from Ref. [47] implemented here in Abaqus to model the AlSi12 matrix behavior.

Stress [MPa]	300	310	330	350	360	370	375	379	382
Plastic strain	0	0.01	0.02	0.03	0.04	0.05	0.06	0.07	0.08

Table 4
Density of the ungraded AlSi12/Al_2O_3 and AlSi12/SiC composites measured by the Archimedes method.

Material	Theoretical density, TD [g/cm^3]	Measured density [g/cm^3]	Relative density [%TD]
AlSi12 + 10%Al_2O_3	2.787	2.778	99.676
AlSi12 + 20%Al_2O_3	2.918	2.913	99.812
AlSi12 + 30%Al_2O_3	3.050	3.038	99.609
AlSi12 + 10%SiC	2.706	2.698	99.704
AlSi12 + 20%SiC	2.762	2.750	99.566
AlSi12 + 30%SiC	2.818	2.804	99.503

densities necessary to calculate the relative densities of the composites were determined using the density of AlSi12 = 2.656 g/cm^3, which was calculated from the densities of Al = 2.7 g/cm^3 and Si = 2.33 g/cm^3, respectively. The density of Al_2O_3 = 3.95 g/cm^3 was obtained from the measurements on pure alumina sinter consolidated in the hot press at 1450 °C/1h/30 MPa, which resulted in a fully dense material. The immersion liquid was distilled water at a temperature of 22 °C, with a density of 0.9978 g/cm^3.

2.4. Measurement of thermal residual stresses

The ungraded AlSi12/Al_2O_3 and AlSi12/SiC composites as well as the three-layer FGMs considered in this work are bulk materials. Therefore, the neutron diffraction (ND) technique was used to evaluate the thermal residual stresses in these materials due to its significant penetration depth. When measuring TRS by diffraction methods, whether X-ray diffraction or neutron diffraction, it is important to remember that residual stresses are not measured directly. In these methods, the measurable property is the interplanar distance *d*. To determine the deformation of the crystalline lattice, we compare the measured interplanar distances in the sintered composites with the measured interplanar distances in the residual stress-free materials (starting powders). Combining Bragg's law $\lambda = 2d\sin\theta$ and the relation $d = 2\pi/q$, the elastic strains due to residual stress can be calculated as

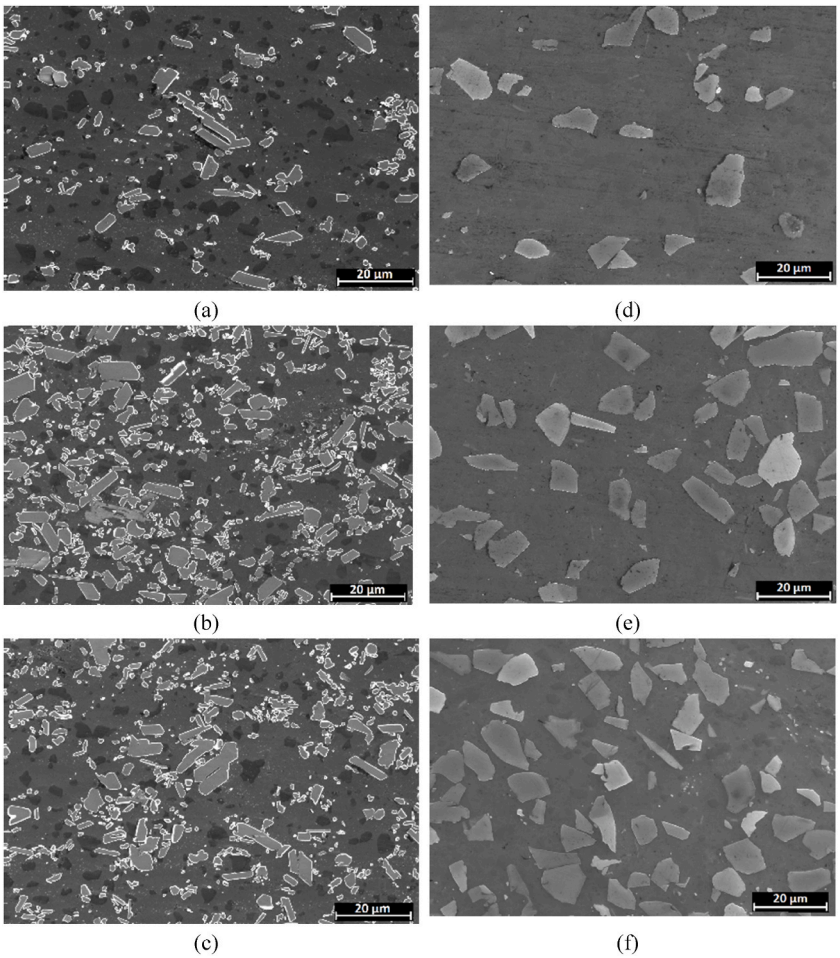

Fig. 6. SEM - secondary electron detector images of AlSi12/Al_2O_3 composites with (a) 10 %, (b) 20 %, (c) 30 % of Al_2O_3, and AlSi12/SiC composites with (d) 10 %, (e) 20 %, and (f) 30 % of SiC. The magnification is 1000x.

$$\varepsilon_i = \frac{d_i - d_0}{d_0} = \frac{q_0}{q_i} - 1, \mathrm{i} = \mathrm{x}, \mathrm{y}, \mathrm{z} \tag{1}$$

where d_0 is the interplanar distance between the lattice planes obtained from the ND measurements on pure Al_2O_3 powder (reference state), q_0 is the corresponding Bragg peak position in the reciprocal space obtained from the powder measurements, d_i are the measured interplanar distances in *x, y, z* directions, q_i are the corresponding Bragg peak positions in these directions.

Once the deformations in the tested materials are determined from Eq. (1), the thermal residual stresses can be calculated using the Hooke's law (Eqs (2)–(4)).

$$\sigma_x = \frac{E}{(1-2\nu)(1+\nu)}\left[(1-\nu)\varepsilon_x + \nu\left(\varepsilon_y + \varepsilon_z\right)\right] \tag{2}$$

$$\sigma_y = \frac{E}{(1-2\nu)(1+\nu)}\left[(1-\nu)\varepsilon_y + \nu(\varepsilon_x + \varepsilon_z)\right] \tag{3}$$

$$\sigma_z = \frac{E}{(1-2\nu)(1+\nu)}\left[(1-\nu)\varepsilon_z + \nu\left(\varepsilon_x + \varepsilon_y\right)\right] \tag{4}$$

It should be mentioned that in the above equations and the numerical modeling of residual stresses (Section 2.4), isotropic mechanical properties were assumed for both the matrix and the reinforcing ceramic materials. While this assumption is reasonable for the AlSi12 matrix, it may not hold for Al_2O_3 and SiC having in mind that monocrystals of these ceramic materials are anisotropic [42, 43]. However, when multiple ceramic crystals are randomly oriented, as it is the case for the sintered Al_2O_3 and SiC grains (crystallites) in the composites studied, it seems plausible to assume isotropic behavior for the ceramic reinforcements as well [44,45].

The neutron diffraction experiments were conducted using the pulse overlap time-of-flight diffractometer POLDI at the Swiss

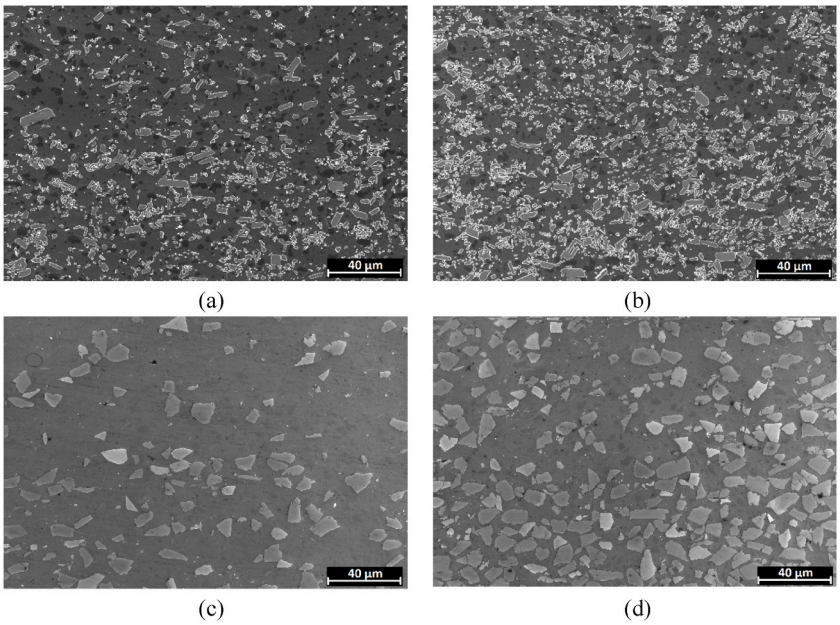

Fig. 7. SEM - secondary electron detector images of the interlayer regions in the FGMs between the following layers: (a) AlSi12 + 10%Al_2O_3 and AlSi12 + 20%Al_2O_3, (b) AlSi12 + 20%Al_2O_3 and AlSi12 + 30%Al_2O_3, (c) AlSi12 + 10%SiC and AlSi12 + 20%SiC, (d) AlSi12 + 20%SiC and AlSi12 + 30%SiC. The upper layers are always those with the lower ceramic volume fraction. The magnification for all images is 500x

continuous spallation neutron source SINQ in Villigen PSI. Measurements were taken at five points on the specimens, in three orthogonal directions – one normal (radial) and two in-plane (axial and hoop) directions, for all the samples, namely: (i) bulk composites AlSi12+xAl_2O_3 (x = 10, 20, 30 vol%), (ii) bulk composites AlSi12+xSiC (x = 10, 20, 30 vol%), (iii) for each composite layer within the three-layer FGM sample AlSi12+xAl_2O_3 (x = 10, 20, 30 vol%), and (iv) for each composite layer within the three-layer FGM sample AlSi12 + xSiC (x = 10, 20, 30 vol%).

2.5. *Numerical modeling of thermal residual stresses*

The numerical model used to determine the residual stresses generated during the manufacturing process of the ungraded composites and the FGMs is based on the actual microstructure of the materials obtained from micro-XCT. Development of a finite element model based on the actual material microstructure involves: (i) micro-XCT imaging, where X-rays are passed through the body from multiple angles, detectors measure the intensity of the X-rays and this data is processed by a computer to produce cross-sectional images (slices) of the internal structures; (ii) image segmentation, which is performed on the micro-XCT scans to identify different materials within the scanned object. This process involves delineating boundaries between different structures or materials of interest within the images; (iii) mesh generation, where the object of interest is divided into small geometric elements, typically triangles or tetrahedra for 3D models, to form a mesh. In micro-XCT based FEM models the segmented XCT images are used to generate the mesh. If a mesh is made of cubic elements, a voxel is represented by one cubic element; (iv) assigning material properties such as density, elasticity, and conductivity to each element based on the properties of the corresponding material identified in the micro-XCT scans; (v) simulation, where the mesh and material properties are defined, and the FEM simulations are performed to analyze the behavior of the object under various conditions. The process of building the model is shown schematically in Fig. 3.

In this paper, the micro-XCT images of the microstructure of the sintered materials are processed using ScanIP/FE software (Simpleware Ltd., Exeter, UK) to obtain a three-dimensional RVE with the reproduced composite microstructure consisting of the AlSi12 matrix and the ceramic reinforcement. The volumes occupied by the two phases in the model correspond to their volumes in the real material, while the use of tetrahedral elements with additional smoothing allows accurate reproduction of the microstructure (Fig. 4).

It can be seen from Fig. 4 that the tetrahedral elements properly represent the microstructure of the material, while the cubic elements lead to a significantly worse representation of the actual composite microstructure. When constructing the numerical mesh models to determine residual stresses in the composites, an accurate representation of the microstructure is the key. An incorrectly constructed finite element mesh can lead to erroneous results from the model. Stress concentrators may appear at unsmoothed grain boundaries and the calculation results can be distorted. The quality of the numerical mesh model used in this work can be evaluated by comparing the volume fraction of the ceramic reinforcement in the actual composite with the volume occupied by the finite elements representing the ceramic material in that composite. This comparison is shown in Table 1. The volume fractions of Al_2O_3 and SiC obtained from the micro-XCT analyses differ only slightly from the nominal values of 10, 20, and 30 vol%.

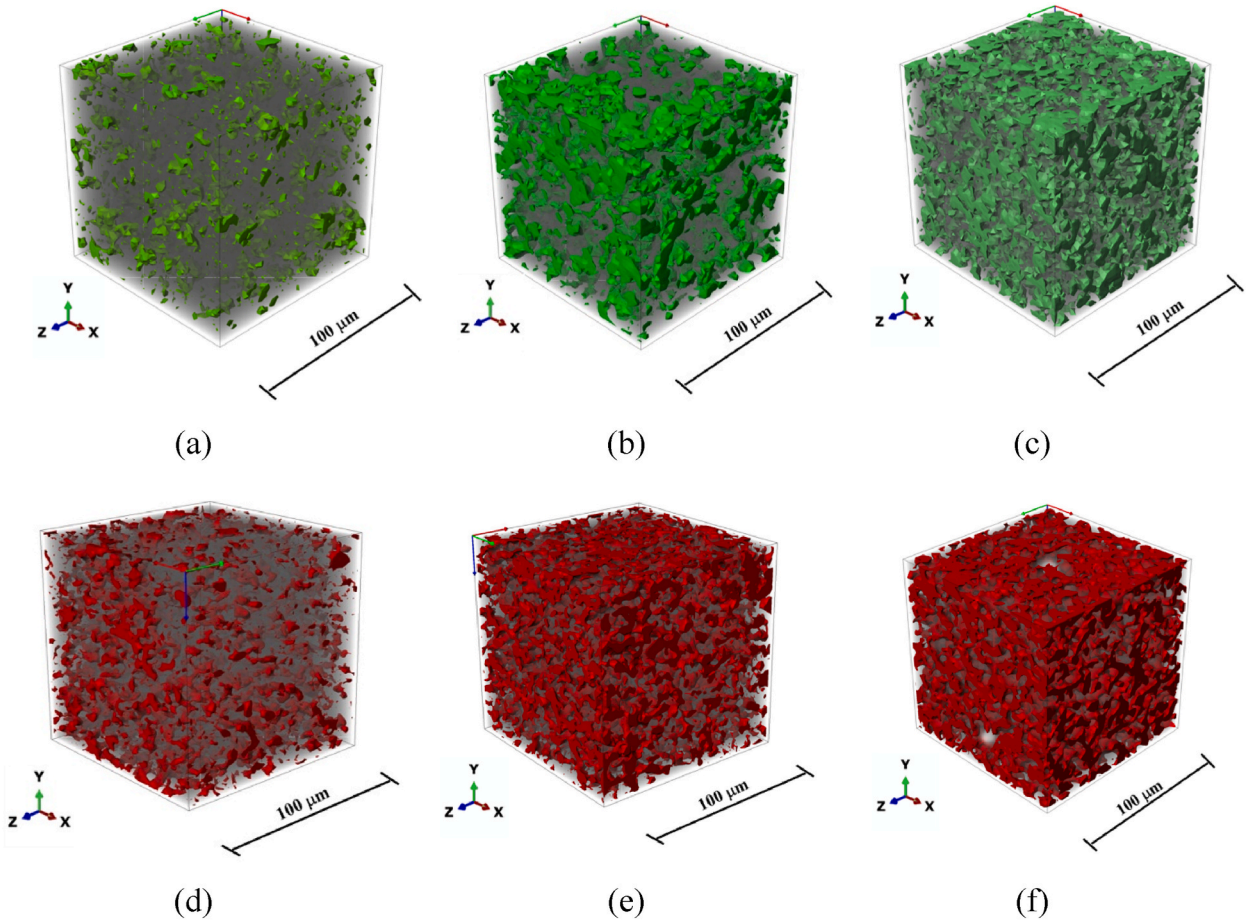

Fig. 8. Segmented images of ungraded composites obtained from micro-XCT characterization: (a)–(c) AlSi12+xAl_2O_3 (x = 10, 20, 30 vol%); (d)–(f) AlSi12+xSiC (x = 10, 20, 30 vol%).

Another issue in stress modeling is the selection of an appropriate model size, i.e., the selection of the RVE size. Different methods for determining the RVE are presented in Ref. [46]. Based on the definitions described there, the following operating scheme is proposed to determine the size of the RVE.

1. Create an FE mesh large enough to match the real microstructure (from SEM images and micro-XCT scans) and preserve the phase volume fractions of the composite; determine the effective elastic properties for the model, such as Young's modulus;
2. Create smaller and smaller FEM meshes, maintaining the phase composition of the composite, and verify that the calculated modulus for such a mesh does not differ from the result obtained for the larger mesh;
3. The smallest mesh that satisfies the above conditions can be considered as the size of the RVE.

According to the procedure described above, a numerical analysis of the effect of the RVE size on the value of effective Young's modulus was performed for AlSi12/SiC composites containing 10, 20, and 30 vol% SiC using meshes with 100 × 100 × 100 μm^3, 75 × 75 × 75 μm^3, 50 × 50 × 50 μm^3, 35 × 35 × 35 μm^3 and 25 × 25 × 25 μm^3. The Young's modulus was calculated from the normal reaction forces along two opposite faces of the sample with prescribed constant normal displacements at the surfaces and otherwise zero tractions (mixed boundary conditions). The modulus was calculated in 3 directions, and the differences in the modulus values were small, less than 3 %. The results of the simulations are shown in Fig. 5 (the average value from 3 directions).

It can be seen from Fig. 5 that the results of the FEM calculations are almost identical for 100x100x100, 75x75x75, and 50x50x50 elements, while they diverge for meshes with a smaller number of elements. Therefore, the size of the RVE is chosen to be 50x50x50 elements, which corresponds to a volume of 50 × 50 × 50 μm^3. The number of inclusions found to be sufficient for RVE is estimated as 25, 45 and 60 for 10 , 20 and 30 vol% of ceramic phase content, respectively.

Based on previous experience [20], a linear elastic material model is used for the ceramic reinforcements in the numerical simulations, while an elastic-plastic material behavior is assumed for the AlSi12 matrix. The material data used in the numerical calculations are listed in Table 2.

The elasto-plastic behavior of the AlSi12 matrix was modeled using the experimental stress–strain curve from Chen et al. [47] and

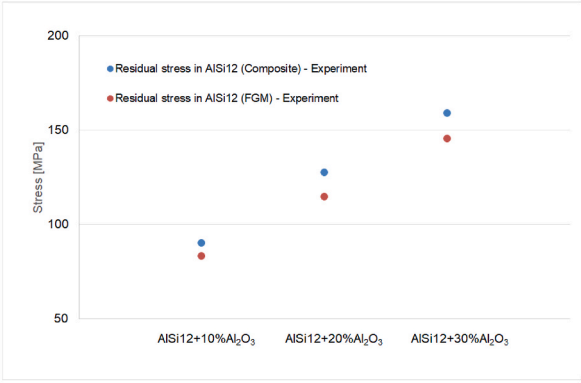

(a)

(b)

Fig. 9. Results of TRS measurements for AlSi12/Al_2O_3 materials: (a) AlSi12 matrix in the ungraded AlSi12+xAl_2O_3 (x = 10, 20, 30 vol%) composites vs. AlSi12 matrix in the FGM; (b) Al_2O_3 reinforcement in the ungraded AlSi12+xAl_2O_3 (x = 20, 30 vol%) composites vs. Al_2O_3 reinforcement in the FGM.

implementing it directly into the Abaqus program. The parameters in Table 3 were determined in Ref. [47] for room temperature. In general, the behavior of the AlSi12 alloy is temperaturedependent, but this has not been considered at the present stage.

In order to model the cooling process from $T_{hot} = 500\ ^\circ C$ to RT (20 °C) in the mold, the following boundary conditions are assumed.

- Step 1: All surfaces are blocked and a pressure of 30 MPa is applied on the top surface. A predefined temperature field is assumed (hot pressing);
- Step 2: All surfaces are blocked and the pressure of 30 MPa is removed. A predefined RT field is applied (cooling in the mold);
- Step 3: All surfaces of the sample are unblocked except for the bottom surface (sample removal after cooling).

3. Results and discussion

3.1. Microstructure

The SEM images of the ungraded AlSi12/Al_2O_3 and AlSi12/SiC composites are shown in Fig. 6. The distributions of the ceramic reinforcements in both composites are relatively homogeneous. However, the Al_2O_3 grains tend to be elongated, whereas the SiC grains tend to be equiaxed polygonal. This difference in shape should be kept in mind when analyzing the TRS behavior in AlSi12/Al_2O_3 and AlSi12/SiC composites and FGMs later in this section. Due to the carefully selected parameters of the HP process, the porosity of the sintered AlSi12/Al_2O_3 and AlSi12/SiC composite samples is very low (see Table 4) and is not considered in the numerical models of the TRS.

The SEM images of the interlayer regions in the three-layer AlSi12/Al_2O_3 and AlSi12/SiC FGMs are shown in Fig. 7, with the upper layers having the lower ceramic volume fraction. It can be seen that the FGM layers are well bonded and the AlSi12 forms a continuous matrix across the layers. It is essential for heat dissipation during cooling from sintering temperature to RT. The images in Fig. 6 show no pores in the material, and the interface between the ceramic and metal is smooth without gaps.

Micro-XCT scans of the ungraded composites with the Al_2O_3 and SiC reinforcements are shown in Fig. 8. A voxel size of about 1 μm is used for x, y, and z-direction. The volume of interest is 100 × 100 × 100 μm^3.

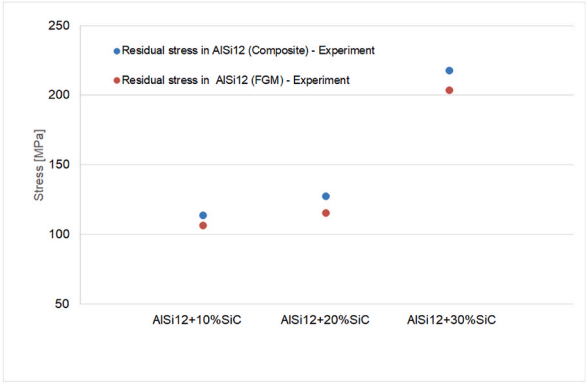

(a)

(b)

Fig. 10. Results of TRS measurements for AlSi12/SiC materials: (a) AlSi12 matrix in the ungraded AlSi12+xSiC (x = 10, 20, 30 vol%) composites vs. the AlSi12 matrix in FGM; (b) SiC reinforcement in ungraded AlSi12+xSiC (x = 20, 30 vol%) composites vs. SiC reinforcement in the FGM.

3.2. Density

The results of the density measurements of the AlSi12+xAl_2O_3 and AlSi12+xSiC (x = 10, 20, 30 vol%) composites are shown in Table 4. As can be seen from the relative density data, both types of composites are very well consolidated, with porosity not exceeding 0.5 %.

3.3. Thermal residual stresses

The results of the TRS measurements are shown in Fig. 9a and b for the alumina-reinforced ungraded composites and the corresponding FGM. Fig. 10a and b shows the TRS data for the silicon carbide-reinforced ungraded composites and the corresponding FGM. Separate graphs show the average TRS in the metal matrix (AlSi12) and the ceramic reinforcement (Al_2O_3 or SiC). Whenever in the figures we refer to the TRS in an FGM, it should be understood as the average TRS in a given layer of that FGM. For example, the red dot in Fig. 9a corresponding to AlSi12 + 20%Al_2O_3 on the x-axis, represents the average TRS in the AlSi12 matrix of the AlSi12 + 20% Al_2O_3 layer within the three-layer AlSi12/Al_2O_3 FGM.

For both materials, the measured stresses in the reinforcing material (Al_2O_3 or SiC) have a negative sign (compressive stresses), and a positive sign (tensile stresses) in the AlSi12 matrix. This is a typical distribution of stress fields resulting from the difference in the coefficients of thermal expansion of the two materials (see Table 1). When the composite material is cooled in an enclosed space, such as the graphite mold used in the sintering process, the metal shrinks, but this process is partially blocked by the ceramic material with a lower coefficient of thermal expansion (creating tensile stresses in the metal). On the other hand, the ceramic material with the lower coefficient of thermal expansion is influenced by the matrix material, which causes additional compression of the ceramic material through greater shrinkage during cooling (creating compressive stresses in the ceramic) [8]. For both Al_2O_3 and SiC-reinforced composites, the same trend can be observed: a higher level of residual stress in the metal matrix (tensile stress) and a higher level of residual stress in the ceramic phase (compressive stress) with the increasing volume fraction of the ceramic.

Stresses in the graded materials are generated in a similar manner. It is worth noting that for both types of reinforcement, Al_2O_3 or SiC, the average residual stresses in the layers of the FGMs (red symbols in Figs. 9 and 10) are lower (regardless of sign) than the stresses in an ungraded composite with the same volume fraction of the ceramic phase (blue symbols in Figs. 9 and 10). This

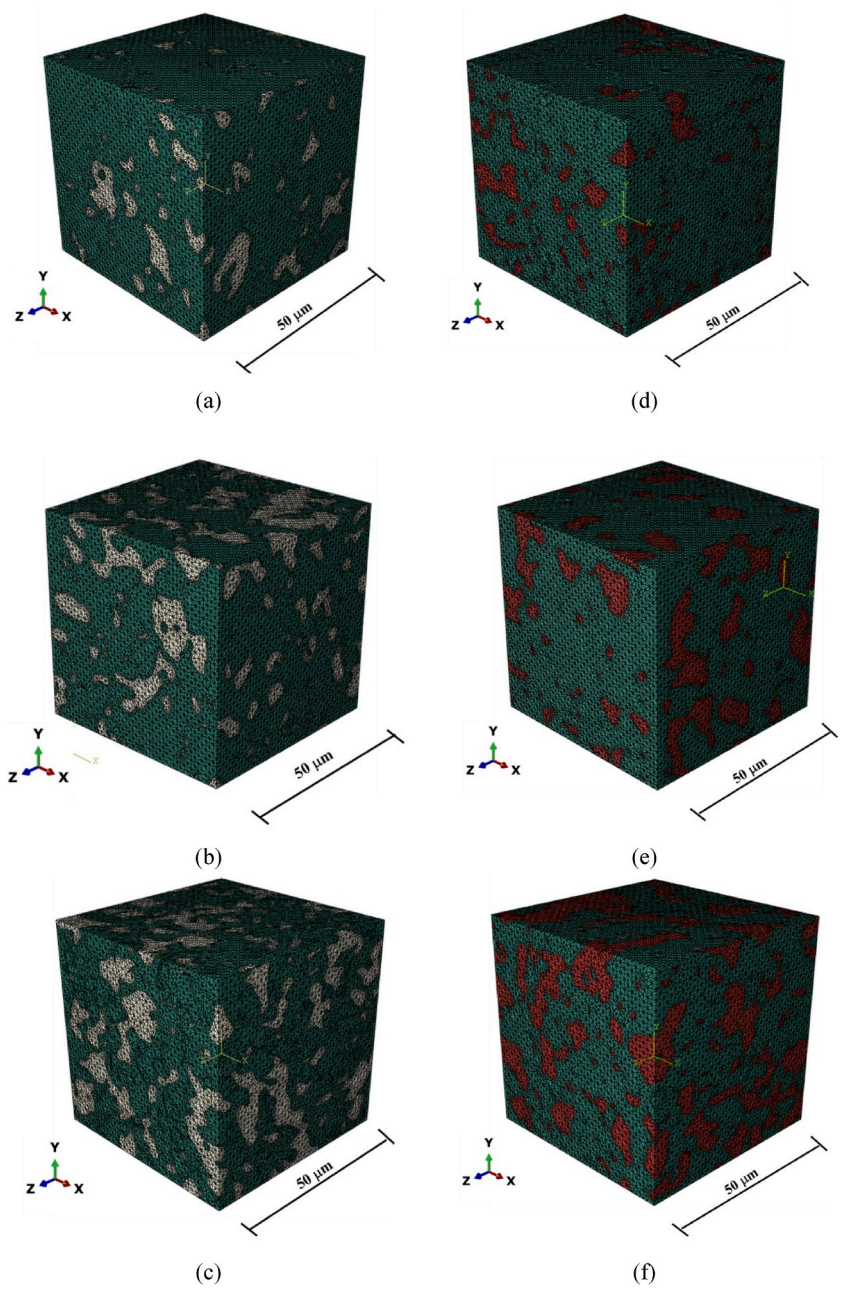

Fig. 11. FE meshes used in the numerical simulations of TRS in the ungraded composites: (a–c) AlSi12+xAl_2O_3 (x = 10, 20, 30 vol%), and (d–f) AlSi12+xSiC (x = 10, 20, 30 vol%).

observation applies to both the AlSi12 matrix and the Al_2O_3 or SiC reinforcements. In addition, a lower level of thermal residual stress is observed in Al_2O_3-reinforced materials (Fig. 9) than in SiC-reinforced materials (Fig. 10). This is due to the smaller difference in coefficients of thermal expansion (CTE) between the AlSi12 matrix and Al_2O_3 compared to AlSi12 and SiC (see Table 2).

An interesting behavior is observed for the TRS in the AlSi12 matrix of the two composites in Figs. 9a and 10a. While for AlSi12+xAl_2O_3 the average TRS in the AlSi12 matrix increases linearly with the increasing volume fraction of alumina (x = 10, 20, 30 vol%), this is not the case for the AlSi12+xSiC (x = 10, 20, 30 vol%) composites, where nonlinear behavior is observed due to a significant jump in TRS in the matrix for AlSi12 + 30%SiC (Fig. 10a). The different values of the coefficients of thermal expansions of Al_2O_3 and SiC are responsible for the higher TRS in AlSi12+xSiC (x = 10, 20, 30 vol%). However, the nonlinearity of TRS in the AlSi12 matrix of AlSi12 + 30%SiC cannot be attributed solely to this difference in the CoEs. A plausible explanation for this effect is the microstructure of both composites, as shown in Fig. 6. It can be seen that the morphology of the two composites is different. In AlSi12/Al_2O_3 samples (Fig. 6a–c) the Al_2O_3 grains are of different sizes, while the AlSi12/SiC samples contain larger SiC grains of similar sizes.

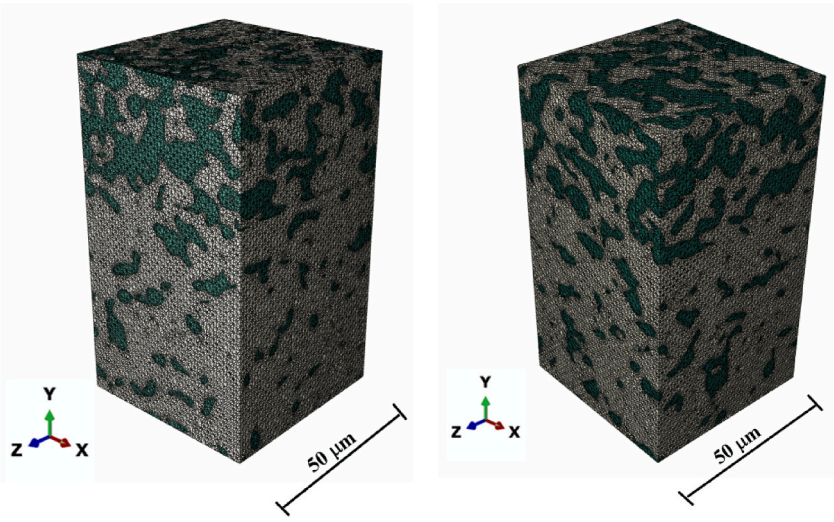

Fig. 12. FE meshes used in the numerical simulations of TRS in the FGMs (a) AlSi12/Al_2O_3, (b) AlSi12/SiC.

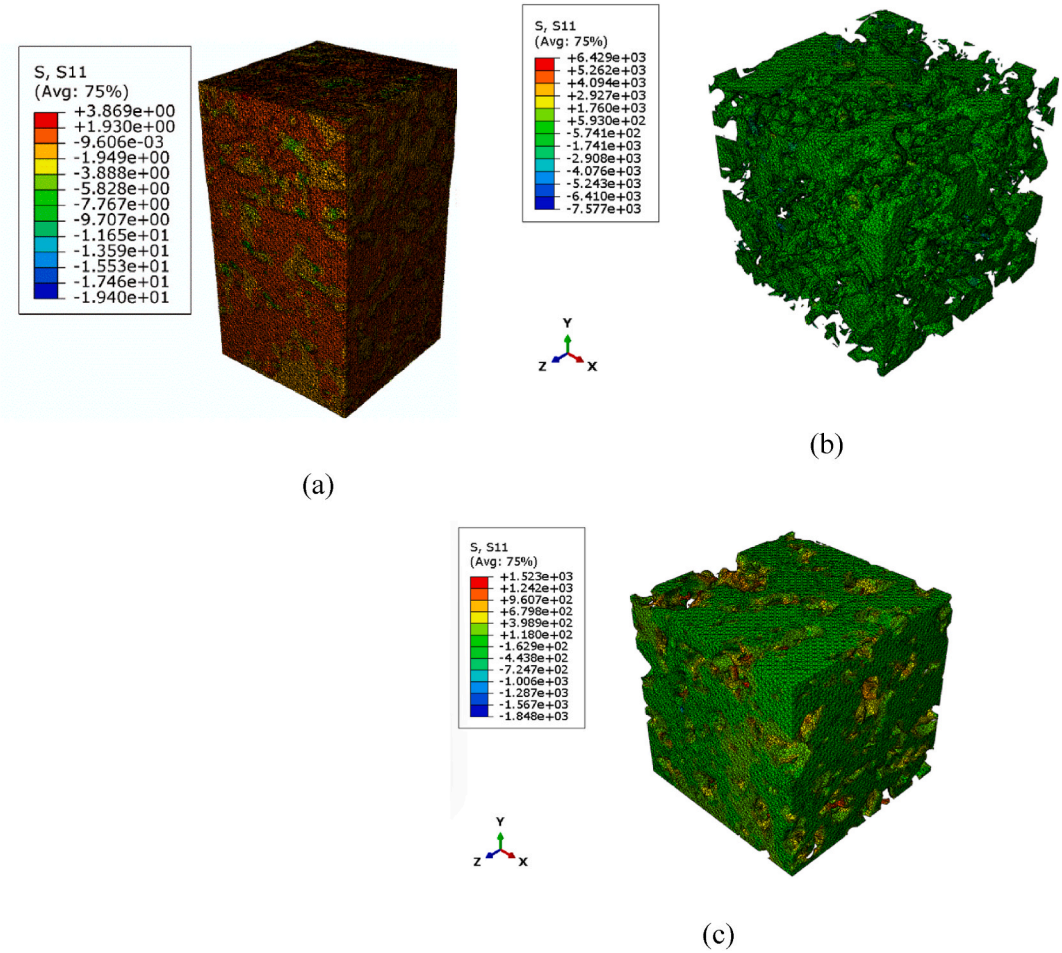

Fig. 13. Examples of TRS distributions in: (a) three-layer FGM AlSi12/Al_2O_3, (b) SiC phase of the ungraded composite AlSi12 + 30%SiC, (c) AlSi12 matrix of the ungraded composite AlSi12 + 30%SiC.

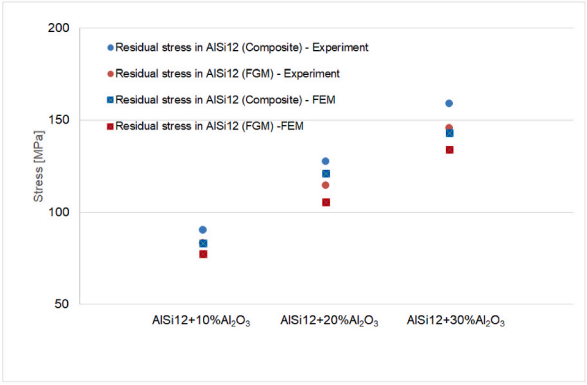

(a)

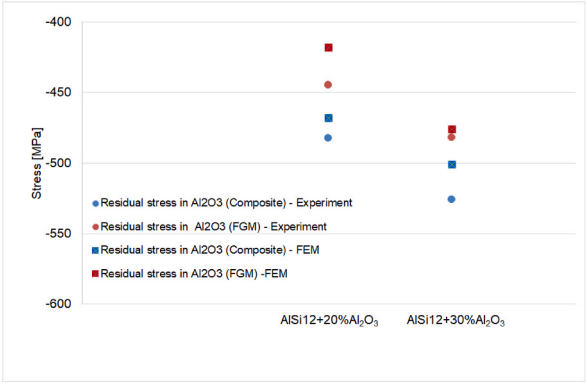

(b)

Fig. 14. Comparison of the thermal residual stress measurements in the AlSi12 matrix (a) and ceramic reinforcement (b) with the FEM results for the ungraded AlSi12+xAl_2O_3 (x = 10, 20, 30 vol%) and the FGM.

It was reported in the literature that grain size and shape of ceramic reinforcement can affect thermal residual stresses in metal-ceramic composites (e.g., Refs. [48,49]). In our work, especially for 30 vol% of SiC, the influence of different shapes and size distributions of SiC grains (Fig. 6f) compared to Al_2O_3 grains (Fig. 6c) may contribute to the observed jump of TRS measured in the AlSi12 matrix (Fig. 10a).

The results of the neutron diffraction measurements in the reinforcement of the ungraded composites and the FGMs with 10 vol% Al_2O_3 and 10 vol% SiC are not shown in Figs. 9b and 10b due to the poor quality of the peaks caused by the low content of the ceramic phase.

3.4. Numerical results and comparison with measured data

Models of thermal residual stresses are prepared for all ungraded composites and FGMs in which the residual stresses were measured by neutron diffraction, namely AlSi12 matrix and xAl_2O_3 reinforcement (x = 10, 20, 30 vol%), AlSi12 matrix and xSiC reinforcement (x = 10, 20, 30 vol%). The figures below show the numerical grids used for the composite materials (Fig. 11a–f) and the FGMs (Fig. 12a and b).

Fig. 13 shows examples of thermal residual stress distributions obtained from the FEM calculations for the FGM with the Al_2O_3 reinforcement (Fig. 13a), as well as for the SiC reinforcement and the AlSi12 matrix of the AlSi12 + 30%SiC ungraded composite (Fig. 13b and c).

The average thermal residual stress in metal or ceramic is calculated as a sum of the average stresses in *j*th elements multiplied by the volume of *j*th element and divided by the total volume of metal or ceramic, respectively [50].

$$\sigma_{ii}^{avr} = \frac{1}{V}\sum_{j=1}^{n}\sigma_{ii}^{j}V_j \tag{5}$$

where n is the number of elements and σ_{ii}^{j} is the stress σ_{xx}, σ_{yy}, and σ_{zz}, in the *j*th element, V_j is the volume of the *j*th element and V is the total volume of metal or ceramic, respectively.

Comparisons of the average TRS measured in the ungraded composites and the FGMs with the average TRS obtained from the numerical models, calculated according to Eq. (5) are shown in Fig. 14a and b and Fig. 15a-b.

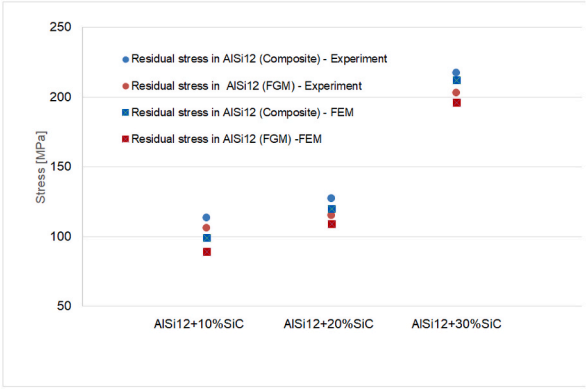

(a)

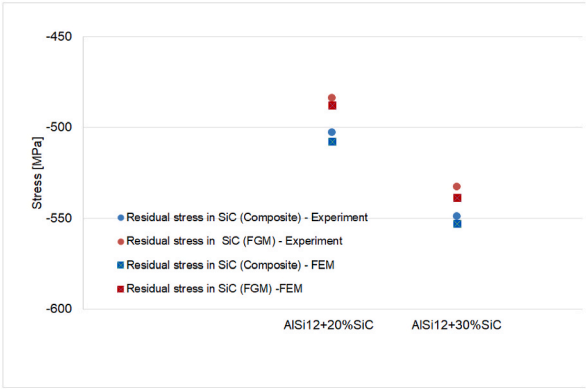

(b)

Fig. 15. Comparison of the thermal residual stress measurements in the AlSi12 matrix (a) and the ceramic reinforcement (b) with the FEM results for the ungraded AlSi12+xSiC (x = 10, 20, 30 vol%) and the FGM.

A comparison between the results from the numerical model based on the actual microstructure and the results from the neutron diffraction measurements shows that the model predicts the experimental data with very good accuracy. The error is less than 5 % for all materials considered. In addition, the FE meshes are based on the micro-XCT images of the actual microstructure of the tested materials, which helped to correctly predict the TRS behavior. In particular, the model properly captures the nonlinear TRS behavior in the AlSi12 matrix of the ungraded and graded AlSi12+xSiC (x = 10, 20, 30 vol%) composites (Fig. 15 a).

4. Conclusions

The main objective of this work was to develop an accurate and reliable numerical model of thermal residual stresses for AlSi12/Al_2O_3 and AlSi12/SiC sintered bulk composites based on the actual material microstructure using micro-XCT data. The numerical results of the average residual stresses predicted by the micro-XCT FEM model were compared with the neutron diffraction data and found to be in close agreement (differences did not exceed 5 %). This accuracy is due to the good quality of the micro-XCT scans and the proper selection of the finite element shape and smoothing technique.

The second objective of this work was to demonstrate that the use of an FGM structure reduces the level of thermal residual stresses in the metal matrix and ceramic reinforcement of the AlSi12/Al_2O_3 and AlSi12/SiC sintered bulk composites. From the analysis of the experimental results shown in Figs. 9 and 10 and the numerical simulations shown in Figs. 14 and 15, it can be seen that the residual stresses in the FGM layers are about 10 % lower than the residual stresses in the corresponding ungraded composites. Residual stresses in functionally graded materials are generally lower than in corresponding ungraded composites due to their gradual variation in composition and properties. The experimental fact reported from our research that the TRS in the ungraded layers is about 10 % higher than TRS in such layers in the FGM can be attributed primarily to gradually changing coefficients of thermal expansion in the FGM [51]. Although our FGMs have a stepwise gradient (layered composite), the fine-tuned process parameters of pressure-assisted sintering make the interfaces between the layers virtually invisible. As a result, there is an almost a smooth transition in material properties, which reduces stress concentrations at interfaces. The lower level of thermal residual stresses in the FGMs compared to the corresponding ungraded composites can have an effect on mechanical properties such as flexural strength and fracture toughness. This may be beneficial for potential applications of the AlSi12 matrix composites, such as brake disc materials in the automotive industry.

CRediT authorship contribution statement

Witold Węglewski: Writing – original draft, Software, Investigation, Data curation, Conceptualization. **Anil A. Sequeira:** Writing – original draft, Software, Investigation. **Kamil Bochenek:** Writing – original draft, Investigation. **Jördis Rosc:** Investigation. **Roland Brunner:** Writing – review & editing, Writing – original draft, Investigation. **Michał Basista:** Writing – review & editing, Writing – original draft, Methodology, Conceptualization.

Declaration of competing interest

The authors declare that they have no known competing financial interests or personal relationships that could have appeared to influence the work reported in this paper.

Data availability

Data will be made available on request.

Acknowledgements

The authors from the Institute of Fundamental Technological Research, Polish Academy of Sciences acknowledge the financial support from the National Science Centre, Poland, within the research project no.2019/35/B/ST8/03131. The residual stress measurements were performed at the Swiss spallation neutron source SINQ, Paul Scherrer Institute, Villigen, Switzerland (Proposal no. 20212674).

The authors from the Materials Center Leoben gratefully acknowledge the financial support under the scope of the COMET program within the K2 Center "Integrated Computational Material, Process and Product Engineering (IC-MPPE)" (Project No 886385). This program is supported by the Austrian Federal Ministries for Climate Action, Environment, Energy, Mobility, Innovation and Technology (BMK) and for Labour and Economy (BMAW), represented by the Austrian Research Promotion Agency (FFG), and the federal states of Styria, Upper Austria and Tyrol.

References

[1] N.A. Travitzky, Effect of metal volume fraction on the mechanical properties of alumina/aluminum composites, J. Mater. Sci. 36 (2001) 4459–4463.
[2] M.B.N. Shaikh, T. Aziz, S. Arif, A.H. Ansari, P.G. Karagiannidis, M. Uddin, Effect of sintering techniques on microstructural, mechanical and tribological properties of Al-SiC composites *Surfaces and Interfaces* 20 (2020) 100598.
[3] M. Rahimian, N. Ehsani, N. Parvin, H.R. Baharvandi, The effect of sintering temperature and the amount of reinforcement on the properties of Al–Al2O3 composite, Mater. Des. 30 (2009) 3333–3337.
[4] S. Li, D. Xiong, M. Liu, S. Bai, X. Zhao, Thermophysical properties of SiC/Al composites with three dimensional interpenetrating network structure, Ceram. Int. 40 (2014) 7539–7544.
[5] P. Gudlur, A. Forness, J. Lentz, M. Radovic, A. Muliana, Thermal and mechanical properties of Al/Al_2O_3 composites at elevated temperatures, Mater. Sci. Eng., A 531 (2012) 18–27.
[6] B. Leszczyńska-Madej, D. Garbiec, M. Madej, Effect of sintering temperature on microstructure and selected properties of spark plasma sintered Al-SiC composites, Vacuum 164 (2019) 250–255.
[7] P.J. Withers, M.J. Roy, in: Peter W.R. Beaumont, Carl H. Zweben (Eds.), Residual Stresses in Metal Matrix Composites *Comprehensive Composite Materials II*, Elsevier, 2018, pp. 275–286.
[8] L.C.R. Schneider, M.E. Fitzpatrick, M.R. Daymond, S.V. Hainsworth, A.C.F. Cocks, Measurement of residual stress in a powder metallurgy aluminium-SiC composite, J. Neutron Res. 12 (2004) 129–133.
[9] P. Vijaya Kumar, D. Jebakani, C. Velmurugan, V. Senthilkumar, Effect of SiC on Mechanical and Microstructural Characteristics of Al Based Functionally Graded Material *Silicon*, vol. 14, 2022, pp. 1247–1252.
[10] M. Marciszko, A. Baczmański, K. Wierzbanowski, M. Wróbel, C. Braham, J.P. Chopart, A. Lodini, J. Bonarski, L. tarkowski, N. Zazi, Application of multireflection grazing incidence method for stress measurements in polished Al–Mg alloy and CrN coating, Appl. Surf. Sci. 266 (2013) 256–267.
[11] R. Fernández, S. Cabeza, T. Mishurova, P. Fernández-Castrillo, G. González-Doncel, G. Bruno, Residual stress and yield strength evolution with annealing treatments in an age-hardenable aluminum alloy matrix composite, Mater. Sci. Eng., A 731 (2018) 344–350.
[12] F. Fiori, E. Girardin, A. Giuliani, T. Lorentzen, A. Pyzalla, F. Rustichelli, V. Stanic, Neutron diffraction measurements for the determination of residual stresses in MMC tensile and fatigue specimens, Phys. B Condens. Matter 923 (4) (2000) 276–278.
[13] N. Noguchi, A. Abduriyim, I. Shimizu, N. Kamegata, S. Odake, H. Kagi, Imaging of internal stress around a mineral inclusion in a sapphire crystal: application of micro-Raman and photoluminescence spectroscopy, J. Raman Spectrosc. 44 (2013) 147–154.
[14] A. Baczmanski, C. Braham, W. Seiler, N. Shiraki, Multi-reflection method and grazing incidence geometry used for stress measurement by X-ray diffraction, Surf. Coat. Technol. 182 (2004) 43–54.
[15] M. Krajewski, W. Węglewski, K. Bochenek, A. Wysmołek, M. Basista, Optical measurements of thermal residual stresses in alumina reinforced with chromium, J. Appl. Phys. 125 (2019), 135104-1-10.
[16] W. Węglewski, M. Krajewski, K. Bochenek, P. Denis, A. Wysmołek, M. Basista, Anomalous size effect in thermal residual stresses in pressure sintered alumina-chromium composites, Mater. Sci. Eng., A 762 (2019) 138111.
[17] V. Parameswaran, A. Shukla, Processing and characterization of a model functionally gradient material, J. Mater. Sci. 35 (2000) 21–29.
[18] Ishibashi H, Tobimatsu H, Matsumoto T, Hayashi K, Tomsia A P, Saiz E and Sio M/Characterization of Mo-SiO 2 Functionally Graded Materials.
[19] N. Araki, D.W. Tang, A. Ohtani, Evaluation of thermophysical properties of functionally graded materials, Int. J. Thermophys. 27 (2006) 209–219.
[20] J. Maj, M. Basista, W. Węglewski, K. Bochenek, A. Strojny-Nędza, K. Naplocha, T. Panzner, M. Tatarková, F. Fiori, Effect of microstructure on mechanical properties and residual stresses in interpenetrating aluminum-alumina composites fabricated by squeeze casting, Mater. Sci. Eng. A 715 (2018) 154–162.
[21] D. Eshelby, The determination of the elastic field of an ellipsoidal inclusion and related problems, Proc. R. Soc. A 241 (1957), 376–396.
[22] C.H. Hsueh, P.F. Becher, Residual thermal stresses in ceramic composites. Part I: with ellipsoidal inclusions *Materials Science and Engineering: a* 212 (1996) 22–28.
[23] C.H. Hsueh, P.F. Becher, Residual thermal stresses in ceramic composites, Part II: with short fibers *Materials Science and Engineering: a* 212 (1996) 29–35.

[24] M. Dao, P. Gu, A. Maewal, R.J. Asaro, A micromechanical study of residual stresses in functionally graded materials, Acta Mater. 45 (1997) 3265–3276.
[25] Z.Y. Ou, D.X. Lei, Analytical solutions for residual stresses of functionally graded medium with inhomogeneity, Key Eng. Mater. 1294 (7) (2007) 353–358.
[26] F. Bouafia, B. Serier, B.A.B. Bouiadjra, Finite element analysis of the thermal residual stresses of SiC particle reinforced aluminum composite, Comput. Mater. Sci. 54 (2012) 195–203.
[27] O. Sayman, F. Sen, E. Celik, Y. Arman, Thermal stress analysis of Wc–Co/Cr–Ni multilayer coatings on 316L steel substrate during cooling process, Mater. Des. 30 (2009) 770–774.
[28] Q. Liu, M. Sun, X. Sun, B. Liu, M. Ostadhassan, W. Huang, X. Chen, Z. Pan, Pore network characterization of shale reservoirs through state-of-the-art X-ray computed tomography: a review *Gas Science and Engineering* 113 (2023) 204967.
[29] T. Vorauer, J. Schöggl, S.G. Sanadhya, M. Poluektov, W.D. Widanage, L. Figiel, S. Schädler, B. Tordoff, B. Fuchsbichler, S. Koller, R. Brunner, Impact of solid-electrolyte interphase reformation on capacity loss in silicon-based lithium-ion batteries, Commun Mater 4 (2023) 44.
[30] V. Schemenz, A. Gjardy, F.F. Chamasemani, A. Roschger, P. Roschger, P. Zaslansky, L. Helfen, M. Burghammer, P. Fratzl, R. Weinkamer, R. Brunner, B.M. Willie, W. Wagermaier, Heterogeneity of the osteocyte lacuno-canalicular network architecture and material characteristics across different tissue types in healing bone, J. Struct. Biol. 212 (2020) 107616.
[31] T. Vorauer, P. Kumar, C.L. Berhaut, F.F. Chamasemani, P.-H. Jouneau, D. Aradilla, S. Tardif, S. Pouget, B. Fuchsbichler, L. Helfen, S. Atalay, W.D. Widanage, S. Koller, S. Lyonnard, R. Brunner, Multi-scale quantification and modeling of aged nanostructured silicon-based composite anodes, Commun. Chem. 3 (2020) 141.
[32] A. Wijaya, B. Eichinger, F.F. Chamasemani, B. Sartory, R. Hammer, V. Maier-Kiener, D. Kiener, M. Mischitz, R. Brunner, Multi-method characterization approach to facilitate a strategy to design mechanical and electrical properties of sintered copper, Mater. Des. 197 (2021) 109188.
[33] J. Nafar Dastgerdi, B. Anbarlooie, A. Miettinen, H. Hosseini-Toudeshky, H. Remes, Effects of particle clustering on the plastic deformation and damage initiation of particulate reinforced composite utilizing X-ray CT data and finite element modeling, Compos. B Eng. 153 (2018) 57–69.
[34] H.J. Lim, H. Choi, G.J. Yun, Multiscale failure and damage analysis of sheet molding compound (SMC) composites using Micro-CT image-based reconstruction model, Compos. B Eng. 231 (2022) 109593.
[35] F. Mesquita, Y. Swolfs, S.V. Lomov, L. Gorbatikh, In-situ synchrotron computed tomography tensile testing observations of the hybrid effect: a comparison with theory, Compos. B Eng. 235 (2022) 109765.
[36] H. Amani Hamedani, M. Baniassadi, A. Sheidaei, F. Pourboghrat, Y. Rémond, M. Khaleel, H. Garmestani, Three-dimensional reconstruction and microstructure modeling of porosity-graded cathode using focused ion beam and homogenization techniques, Fuel Cell. 14 (2014) 91–95.
[37] L. Padurariu, F.F. Chamasemani, R. Brunner, L.P. Curecheriu, V.A. Lukacs, R.S. Stirbu, C.E. Ciomaga, L. Mitoseriu, Analysis of local vs. macroscopic properties of porous $BaTiO_3$ ceramics based on 3D reconstructed ceramic microstructures, Acta Mater. 255 (2023) 119084.
[38] M. Basista, W. Węglewski, K. Bochenek, Z. Poniżnik, Z. Nowak, Micro-CT finite element analysis of thermal residual stresses and fracture in metal-ceramic composites, Adv. Eng. Mater. 19 (2017), 1600725-1-9.
[39] W. Węglewski, M. Basista, M. Chmielewski, K. Pietrzak, Modeling of thermally induced damage in the processing of Cr–Al2O3 composites, Compos. B Eng. 43 (2012) 255–264.
[40] W. Węglewski, M. Basista, A. Manescu, M. Chmielewski, K. Pietrzak, T. Schubert, Effect of grain size on thermal residual stresses and damage in sintered chromium–alumina composites: measurement and modeling, Compos. B Eng. 67 (2014) 119–124.
[41] W. Węglewski, K. Bochenek, M. Basista, T. Schubert, U. Jehring, J. Litniewski, S. Mackiewicz, Comparative assessment of Young's modulus measurements of metal–ceramic composites using mechanical and non-destructive tests and micro-CT based computational modeling, Comput. Mater. Sci. 77 (2013) 19–30.
[42] F. Konstantiniuk, M. Tkadletz, C. Kainz, C. Czettl, N. Schalk, Mechanical properties of single and polycrystalline α-Al_2O_3 coatings grown by chemical vapor deposition, Surf. Coat. Technol. 410 (2021) 126959.
[43] V.I. Ivashchenko, P.E.A. Turchi, V.I. Shevchenko, Simulations of the mechanical properties of crystalline, nanocrystalline, and amorphous SiC and Si, Phys. Rev. B 75 (2007) 085209.
[44] V.E. Saouma, S.-Y. Chang, O. Sbaizero, Numerical simulation of thermal residual stress in Mo- and FeAl-toughened Al_2O_3, Compos. B Eng. 37 (2006) 550–555.
[45] A. Manes, M. Giglio, Microstructural numerical modeling of Al_2O_3/Ti composite, Procedia Struct. Integr. 8 (2018) 24–32.
[46] C. Pelissou, J. Baccou, Y. Monerie, F. Perales, Determination of the size of the representative volume element for random quasi-brittle composites, Int. J. Solid Struct. 46 (2009).
[47] Y. Chen, A.H. Clausen, O.S. Hopperstad, M. Langseth, Stress–strain behaviour of aluminium alloys at a wide range of strain rates, Int. J. Solid Struct. 46 (2009) 3825–3835.
[48] J. Chen, Y. Yang, H. Lu, X. Liu, H. Wang, X. Song, Mechanical behavior of cermets with different morphology of ceramic grains, Acta Mater. 266 (2024) 119649.
[49] K. Seol, A.D. Krawitz, J.W. Richardson, C.M. Weisbrook, Effects of WC size and amount on the thermal residual stress in WC–Ni composites *Materials Science and Engineering: a* 398 (2005) 15–21.
[50] A. Ewert, B. Drach, K. Vasylevskyi, I. Tsukrov, Predicting the overall response of an orthogonal 3D woven composite using simulated and tomography-derived geometry, Compos. Struct. 243 (2020) 112169.
[51] K.S. Ravichandran, Thermal residual stresses in a functionally graded material system *Materials Science and Engineering: a* 201 (1995) 269–276.